ELSEVIER

Contents lists available at ScienceDirect

Journal of the European Ceramic Society

journal homepage: www.elsevier.com/locate/jeurceramsoc





Grain size dependent indentation response of single-phase (CoCuMgNiZn)O high entropy oxides

Justin Cortez^a, Alexander D. Dupuy^{a,b}, Hasti Vahidi^a, Olivia K. Donaldson^a, William J. Bowman^a, Timothy J. Rupert^a, Julie M. Schoenung^{a,c,*}

- ^a Department of Materials Science and Engineering, University of California, Irvine, CA 92697, USA
- ^b Department of Materials Science and Engineering, University of Connecticut, Storrs, CT 06268, USA
- c Department of Materials Science & Engineering and J. Mike Walker '66 Department of Mechanical Engineering, Texas A&M University, College Station, TX 77840, USA

ARTICLE INFO

Keywords: High entropy oxides Spark plasma sintering Mechanical behavior Hall-Petch relationship Inverse Hall-Petch Nanoindentation

ABSTRACT

Vickers indentation and nanoindentation methods were used to explore the hardness, elastic modulus, and fracture toughness of single-phase (CoCuMgNiZn)O transition metal high entropy oxides. Bulk samples with grain sizes ranging from $0.075\,\mu m$ to $1.4\,\mu m$ were consolidated using spark plasma sintering. Measurements reveal relatively small differences in elastic modulus and comparable hardness to Rule-of-Mixture calculations, alluding to minimal effects of entropy stabilization on mechanical properties. Hardness values exhibit a Hall-Petch relationship until an average grain size of $0.11\,\mu m$. Below this grain size an Inverse Hall-Petch relationship is observed with values decreasing up to 70 %. The measured hardness deviates from calculations of hardness using a grain interior-grain boundary composite model, indicating that other mechanisms, such as nanocracking or grain boundary sliding, contribute to the decrease in hardness at smaller grain sizes. Variations in elastic modulus are attributed to grain boundary effects, and variations in fracture toughness are attributed to the absence of grain bridging and transgranular fracture at smaller grain sizes. This grain-size dependent mechanical behavior, which is similar to behavior in MgO, must be controlled when designing (CoCuMgNiZn)O materials for various applications.

1. Introduction

High entropy stabilization of single-phase materials has emerged as a promising design strategy in the development of novel materials. In 2004, Cantor et al. developed an equiatomic multicomponent alloy composed of Cr, Mn, Fe, Co, and Ni that exhibited an unexpected singlephase FCC structure [1]. The structures anticipated by scientists of the time were either metallic glass or the formation of many intermetallic compounds [2,3]. Therefore, the appearance instead of a solid solution material garnered much interest, as evidenced by the significant increase in publication rate for multicomponent alloys during the following years [4,5]. Yeh et al. were the first to coin these equiatomic multicomponent alloys as "high entropy alloys" (HEAs) [6]. Inspired by the promise of novel properties and an expanded compositional space, the design principles behind high entropy stabilization have since been applied to ceramic materials. The first high entropy oxide (HEO), (CoCuMgNiZn)O, hereafter referred to as TM-HEO, was discovered by Rost et al. [7]. TM-HEO is composed of five oxide components in

equimolar ratios that form a single-phase rocksalt crystal structure after processing. The single-phase state has been shown to be highly stable, being achievable using a range of synthesis methods such as solid state, combustion, wet chemical, or pyrolysis methods [7–9]. Despite the complexity of these materials, HEOs appear to be single phase and chemically homogeneous down to the atomic level [10,11]. The above studies have prompted others to explore high entropy stabilization in other ceramic materials such as fluorites [12], perovskites [13], and other non-oxide systems [14–16].

The recent interest in these materials is partly due to the exciting properties that can be obtained with access to the expanded compositional space that high entropy stabilization allows. Several studies have revealed that the TM-HEO composition possesses a wide variety of promising properties including low thermal conductivity [17], high electrical storage capacity [18], controllable phase composition [19], and excellent ionic conductivity [20]. Despite considerable interest in HEOs and their functional properties, research into their mechanical properties remains relatively limited. For the above functional

^{*} Correspondence to: 575 Ross St., College Station, TX 77843, USA. E-mail address: schoenung@tamu.edu (J.M. Schoenung).

properties to be widely utilized, a better understanding of the mechanical behavior in HEO materials is also needed. This understanding is particularly crucial for relevant applications such as thermal barrier coatings [17] and batteries [21,22], which require a certain degree of robustness and control of elastic modulus, hardness, and fracture toughness to properly function [23,24].

Microstructure features, such as porosity, phase composition, and grain morphology, can influence the mechanical properties of ceramics [25,26]. Grain size, in particular, is known to significantly affect the mechanical behavior of polycrystalline materials. The well-known Hall-Petch phenomenon describes how mechanical strength is inversely related to the grain size [27,28]. As the grain size decreases, the hardness generally increases due to the grain boundaries acting as barriers to dislocation motion. There is often a limit to this grain boundary strengthening effect, with many materials exhibiting an inverse Hall-Petch relationship at very small grain sizes. A number of different mechanisms have been proposed to explain the inverse Hall-Petch effect in ceramics, such as grain boundary sliding and nanocrack-based deformation [29,30].

Some initial studies in the literature have examined the mechanical properties of TM-HEO, such as elastic modulus, elastic isotropy, hardness, bending strength, and scratch behavior [17,31–35]. For example, elastic modulus measurements conducted on thin film samples using contact resonance atomic force microscopy demonstrated values of 152.0 ± 10.6 GPa [17]. Hong et al. explored the role of grain size on mechanical behavior in bulk sintered samples using three-point bend measurements [31]. They found that grain size influences the elastic modulus, with the modulus ranging from 67 GPa at a grain size of $0.5\,\mu m$, to $108\,GPa$ at a grain size of $3.5\,\mu m$. Wang et al. conducted nanoscratch tests on coarse grain (1.4 μm) and nano grain (0.075 μm) samples [34]. Post-deformation transmission electron microscopy revealed dislocation activity in the coarse grain samples and grain boundary sliding and intergranular cracking in the nano grain samples. While these previous studies are insightful, they are limited in scope. Thus, there is a need for a more robust investigation into the influence of microstructure on the key mechanical properties of hardness, elastic modulus, and fracture toughness in single-phase TM-HEOs. Therefore, in this study we investigate the role of microstructure on the mechanical properties of TM-HEO, by altering sintering parameters to produce bulk single-phase samples with a range of grain sizes. We then use mechanical indentation measurements to explore how grain size influences the hardness, elastic modulus, and fracture toughness in single-phase TM-HEO. We combine these measurements with modeling and electron microscopy characterization to reveal the mechanisms governing changes in mechanical behavior with variations in grain size.

2. Experimental procedure

TM-HEO nanopowders (average particle size on the order of $\sim\!0.050\,\mu m$) were prepared using solid-state synthesis. The starting constituent oxide nanopowders were purchased from US Research Nanomaterials (Houston, TX, USA) as CoO (0.05 μm particle size, 99.7 wt%), CuO (0.022–0.055 μm , 99.95 %), MgO (0.05 μm , 99.95 %), NiO (0.018 μm , 99.98 %), and ZnO (0.018 μm , 99.95 %). These powders were blended in equimolar amounts using a mortar and pestle, followed by planetary ball milling (PBM) using a Premium 7 ball mill (Fritsch GmbH, Idar-oberstein, Germany). The powders were suspended in isopropanol and milled at 300 rpm for 3 hours using silicon nitride jars and media. These blended oxide powders were heat treated at 900°C for 20 minutes to complete the solid-state reaction and form single-phase rocksalt TM-HEO powders. The pre-reacted powders were reground to nano size using the PBM at 450 rpm for 12 hours.

The reacted TM-HEO nanopowders were consolidated into bulk samples using graphite tooling in a Fuji model 825 S (Fuji, Saitama, Japan) spark plasma sintering (SPS) apparatus. The powders were heated to a temperature of 700, 750, 800, 850 or 900 °C at a heating rate

of 200 °C/min, under 100 MPa of pressure. The temperature was held for 5 minutes and then cooled at 50 °C/min while the pressure was slowly reduced to zero. The as-consolidated bulk samples were subsequently polished to 1 µm diamond suspension. Archimedes method was used to determine the density of the bulk consolidated samples. A SmartLab (Rigaku, Tokyo, Japan) X-ray diffractometer (XRD) was used to confirm the phase state of both the TM-HEO powder and bulk consolidated samples. Microstructure analysis was performed using a FEI (Hillsboro, OR, USA) Magellan 400 XHR scanning electron microscope (SEM). Micrographs of fracture surfaces were collected to capture the samples' representative bulk microstructure. The average grain size (AGS) values for each sample were calculated by measuring the major axis of approximately 400 grains observed in several micrographs using the ImageJ software [36]. Fracture surfaces were used as these could be consistently acquired from all of our samples and previous studies have found that grain size measurements from fracture surfaces provide similar information to those acquired from etched surfaces [37].

Hardness measurements were performed using a Duramin (Struers, Cleveland, Ohio) hardness tester with a Vickers diamond indenter. Through trial and error, the optimal maximum load was determined to be 1.96 N for 5 s, which avoids any cracks or chipping that could influence the measurements. An Agilent (Santa Clara, CA, USA) G200 nanoindenter equipped with a diamond Berkovich tip and NanoSuite® software was also used to determine the local hardness and elastic modulus of the bulk consolidated samples. Each sample was indented with a 7×7 array of indents, each using a maximum load of 400 mN with a peak hold of 5 s.

Fracture toughness measurements were performed on the bulk consolidated single-phase TM-HEO samples with the same Duramin hardness tester discussed above using a load of 4.9 N to induce radial cracks. At these higher load values, the test can produce radial cracks in line with the pyramidal shaped indenter, which serve as an indicator of fracture toughness [38,39]. A schematic of a Vickers indent used for fracture toughness measurements is depicted in Fig. 1 A. The variable 'a' is the indent half-diagonal, 'l' is the surface crack length, and 'c' is the length of the indent half-diagonal plus crack length. Figs. 1(B) and 1(C) provide cross sectional views that distinguish a Palmqvist-style crack, which is predicted to occur with a characteristic length ratio of c/a2.5, from a Median-style crack, which occurs when c/a > 2.5. Together with the hardness and elastic modulus values, the length of the radial crack can be used to determine the fracture toughness. The uncertainty estimates for average grain size, hardness, elastic modulus, and fracture toughness were calculated as one standard deviation from the mean.

3. Results

3.1. Microstructure and phase state

XRD analysis of the sintered samples confirms each sample exhibits a single-phase rocksalt structure (Supplemental Figure S1), free of any secondary phases or oxide reduction reactions, similar to previous studies [7,19,31,40]. A summary of the sintering temperature, average grain sizes (AGS), and relative densities of the bulk consolidated single-phase TM-HEO samples is presented in Table 1.

The influence of sintering temperature on AGS) is also illustrated in Fig. 2A. As expected, lower temperatures yield smaller grain sizes (0.075 \pm 0.050 μm), while higher temperatures produce coarser grains (1.4 \pm 0.5 μm). Fig. 2(B-F) show fracture surface micrographs of the consolidated samples, illustrating variations in grain size and morphology. Notably, all samples exhibit densities > 95 %, despite the low sintering temperatures and short consolidation times. It is important to note that voids visible in the fracture surface micrographs (Fig. 2B-F) are not pores, but are instead bulk material that was dislodged during fracture surface preparation.

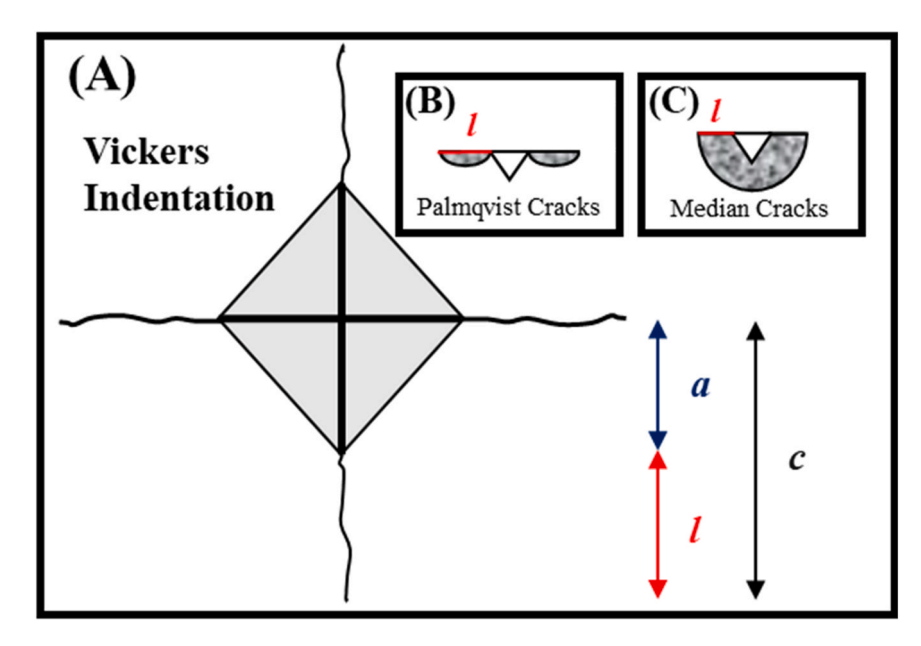


Fig. 1. (A) Schematic of a Vickers style indentation used for fracture toughness measurements displaying the indent half-diagonal a (blue), the crack length l (red), and the combined length c (black). Inset (B) shows the cross section of a Palmqvist style crack with the crack length l, which is predicted to occur with a characteristic length ratio of c/a < 2.5. Inset (C) shows the cross section of a Median style crack with the crack length l, which occurs when c/a > 2.5.

Table 1Summary of the sintering temperature, average grain size, and relative density of the bulk consolidated single-phase TM-HEO samples.

Sample Label	Sintering Temperature (°C)	Average Grain Size (µm)	Relative Density
SPS700	700	0.075 ± 0.050	95.6 %
SPS750	750	0.11 ± 0.08	98.4 %
SPS800	800	0.23 ± 0.11	97.4 %
SPS850	850	0.59 ± 0.26	98.8 %
SPS900	900	1.41 ± 0.55	97.9 %

3.2. Hardness and elastic modulus

Nanoindentation measurements reveal that hardness in the consolidated TM-HEO samples is influenced by grain size, as seen in Fig. 3. Dashed lines are included in Fig. 3 to help guide the reader. The sample with an AGS = $0.075 \, \mu m$ (sample SPS700) exhibits the lowest hardness value in this study (2.9 GPa). The sample with an AGS $= 0.11 \, \mu m$ (sample SPS750) exhibits a large increase in hardness to 10.2 GPa. Hardness then decreases with increasing grain size for AGS values greater than 0.11 µm. Elastic modulus values measured using nanoindentation exhibit a similar trend to the hardness data, as seen in Fig. 3. Sample SPS700, having the smallest grain size (AGS = $0.075 \, \mu m$), exhibits the lowest elastic modulus value in this study (63 GPa). The elastic modulus reaches its highest value of 163 GPa at a grain size of $0.11~\mu m$ (sample SPS750). For samples with AGS values greater than 0.11 μ m, a decrease in elastic modulus values is observed. For AGS = $1.4 \mu m$, our largest grain size (sample SPS900), the consolidated TM-HEO sample exhibits the second lowest elastic modulus value observed in this study (112 GPa).

3.3. Fracture toughness

Fracture toughness values were determined on the basis of the radial cracks on the surface, such as those seen for the indent in Figs. 4A and 5. Interpretation of fracture toughness based on these crack length values depends on the type of cracking present underneath the surface adjacent to and below the indent. One crack type is the Palmqvist crack, which is characterized by half-elliptical cracks that emanate from the edges of the

indent, but do not extend underneath the indent, as illustrated in Fig. 1B. The second crack type is the Median style crack, which forms a halfpenny crack profile around and underneath the indent (Fig. 1 C). As fracture primarily occurs beneath the surface adjacent to and underneath the indent, it is not possible to visually confirm the type of crack system induced during indentation without sectioning the material. However, the crack system can be predicted based on the observed indent geometry and crack length. Zhuang and Niihara have described methods in which the ratios of the 'c'(crack length + indent half-diagonal) and 'a'(indent half-diagonal) values, as depicted in Fig. 1 A, can be used to predict the likely crack type [38,39]. Calculating the c/a ratio provides an indication of the appropriate fracture toughness equation, without requiring invasive sectioning procedures. A value of c/a > 2.5 indicates the presence of half-penny Median style cracking, for which the appropriate Niihara equation [38] for fracture toughness (K_{IC}) is:

$$K_{IC} = 0.0309 \quad \left(\frac{E}{H}\right)^{\frac{2}{5}} \left(\frac{P}{c_{3}^{\frac{3}{2}}}\right)$$
 (1)

where E is elastic modulus, H is hardness, P is load, and c is the crack plus indent half-diagonal length. If c/a is less than 2.5 then Palmqvist style cracking is expected, and the Niihara equation for fracture toughness is:

$$K_{IC} = 0.0123 \left(\frac{E}{H}\right)^{\frac{2}{5}} \left(\frac{H \bullet P}{l}\right)^{\frac{1}{2}} \tag{2}$$

where *l* is the crack length.

The c/a ratio was calculated to identify the cracking style and the correct fracture toughness equation for each sample. Fracture toughness is observed to generally increase with increasing grain size, as seen in Fig. 4B. Sample SPS700 (AGS = 0.075 μ m) exhibits the lowest fracture toughness value of 0.83 \pm 0.04 MPa/(m $^{1/2}$), while sample SPS850 (AGS = 0.59 μ m) exhibits the highest fracture toughness value of 1.88 \pm 0.17 MPa/(m $^{1/2}$).

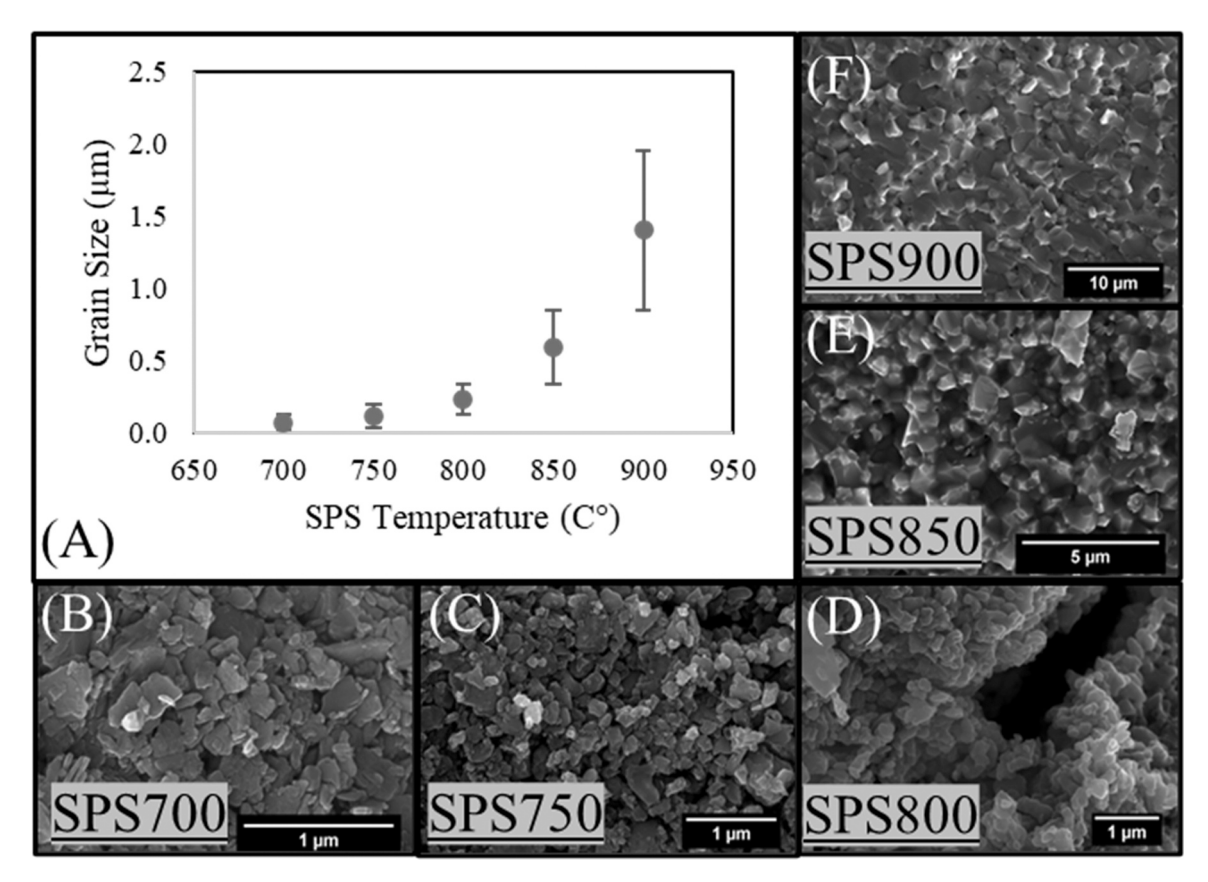


Fig. 2. (A) Measured average grain size values versus sintering temperature used during spark plasma sintering (SPS). (B-F) Scanning electron micrographs of representative fracture surfaces used to measure the average grain size for bulk consolidated single-phase TM-HEO samples sintered at the following temperatures: (B) 700 °C (sample SPS700), (C) 750 °C (SPS750), (D) 800 °C (SPS800), (E) 850 °C (SPS850), and (F) 900 °C (SPS900).

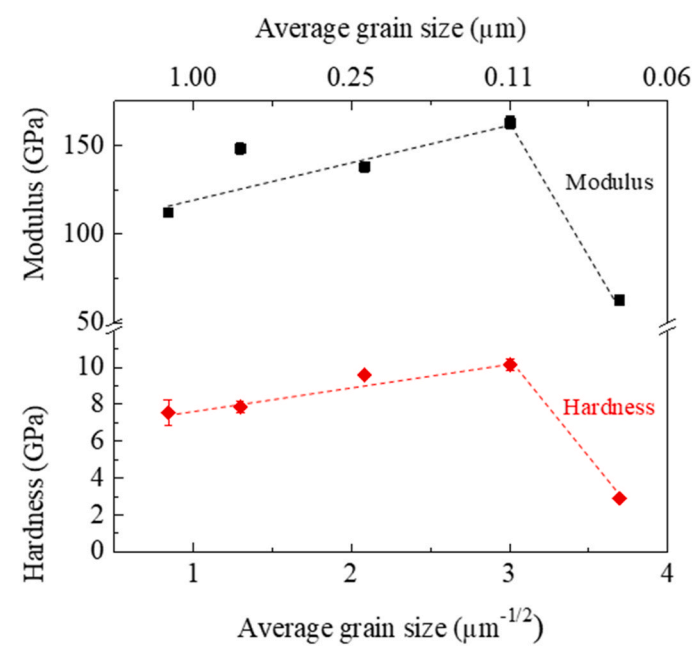


Fig. 3. Elastic modulus (black dataset) and hardness (red dataset) measured from nanoindentation with respect to inverse squared average grain size for bulk consolidated single-phase TM-HEO samples. Error bars for most samples are smaller than the data points presented.

4. Discussion

4.1. Processing and microstructure

Through SPS consolidation of nanocrystalline powders, it was possible to prepare bulk single-phase TM-HEO samples with grain sizes ranging from 0.075 μm to 1.4 μm . The low temperatures and short processing times associated with SPS allow for significant control over the final grain size of our TM-HEO samples. Increasing SPS consolidation temperatures resulted in TM-HEO samples with larger grains (Fig. 2B-F), which is consistent with our previous work [19,40]. These samples, with their wide range of grain sizes, provide an ideal platform for studying the influence of grain size in single-phase TM-HEOs on mechanical behavior. Furthermore, despite the range of processing temperatures and final microstructures, all of our samples exhibit relative densities $>\!95$ %. The high density of the samples allows the mechanical behavior to be explored independent of porosity.

4.2. TM-HEO rule-of-mixtures comparison

Values of hardness and elastic modulus for each of the five constituent oxides were acquired from the literature [32,41,42] as a basis for comparison to the relative mechanical performance of our equimolar, single-phase bulk TM-HEO samples (Fig. 5). From the literature values for the constituent oxides, an estimate of the value for the equimolar TM-HEO is calculated using a Rule-of-Mixtures approach, as also shown in Fig. 5. To facilitate comparison, the range of values measured for our bulk single-phase TM-HEO samples are illustrated with shaded regions in Fig. 5. Specifically, hardness values range from 2.9 \pm 0.1 GPa to 10 \pm 0.2 GPa, and elastic modulus values range from 63 \pm 0.8 GPa to 163 \pm 3.7 GPa. It is important to note that the literature hardness values for the

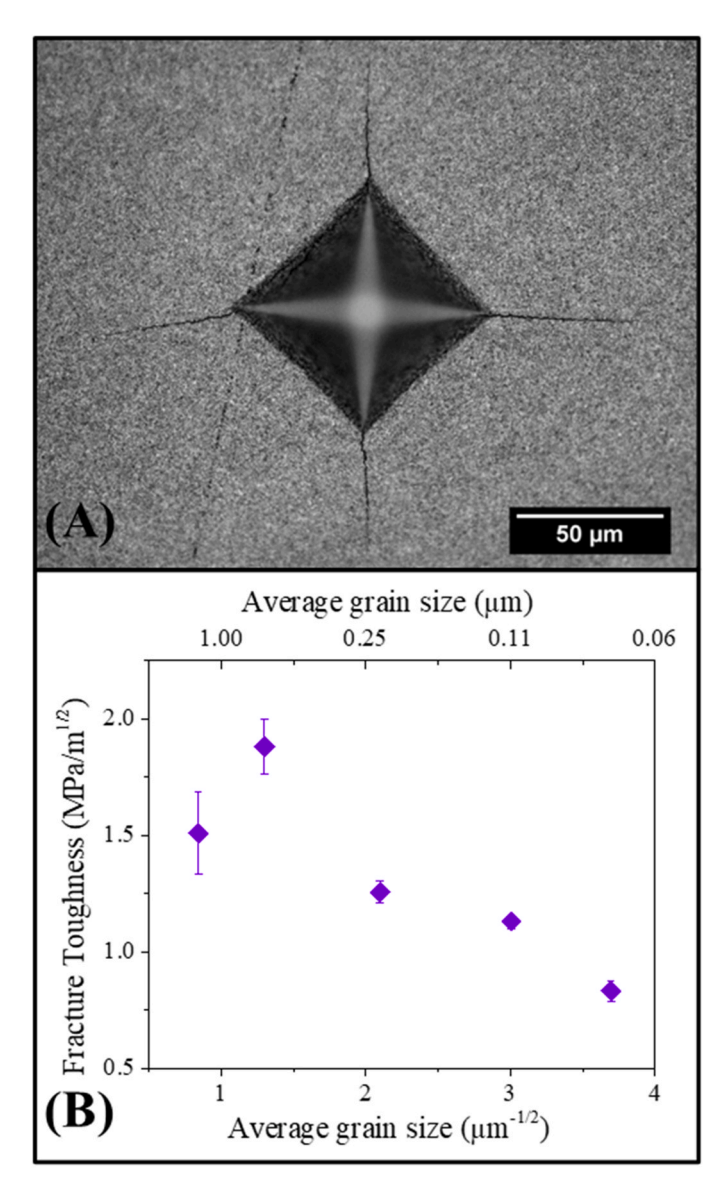


Fig. 4. (A) Example of cracks observed on the surface of a bulk consolidated single-phase TM-HEO sample, induced using a Vickers hardness indenter during a fracture toughness measurement. (B) Fracture toughness versus inverse squared average grain size.

five constituent oxides were measured from samples with a range of different microstructure conditions [41,42], while the literature modulus values were acquired from first-principles calculations [32]. Furthermore, the reader is asked to note the logarithmic scale in Fig. 5. The hardness values for the constituent oxides range from ~2 GPa for CuO [42] to ~13 GPa for MgO [31], yielding a Rule-of-Mixtures value of ~7.45 GPa. In comparison, each of the TM-HEO bulk consolidated single-phase samples, except sample SPS700 (AGS = $0.075 \mu m$), exhibits a hardness value of 7.5 GPa or greater. DFT calculated elastic modulus values for the constituent oxides range from ~122 GPa for CuO to ~287 GPa for MgO [32], yielding a Rule-of-Mixtures value of 176 GPa. The elastic modulus values for our TM-HEO samples are on the same order of magnitude, yet all are slightly less than the Rule-of-Mixtures estimated value. Based on the relatively small difference in elastic modulus and comparable hardness to Rule-of Mixture calculations, entropy stabilization does not seem to have a significant effect on these properties in single-phase TM-HEO.

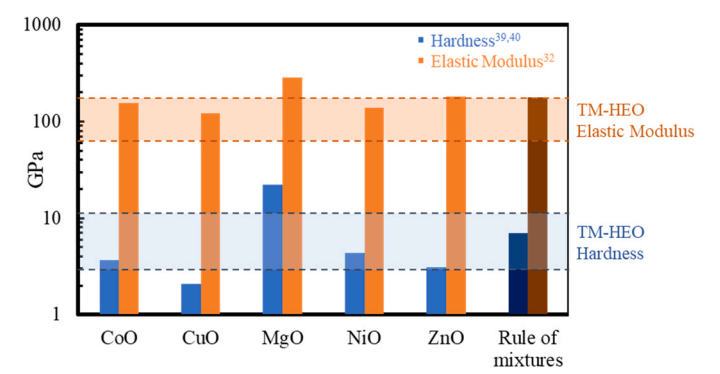


Fig. 5. Literature values for the hardness [41,42] (indentation testing) in blue and elastic modulus [32] (DFT calculation) in orange for the constituent oxides: CoO, CuO, MgO, NiO, and ZnO. Rule-of-mixtures values calculated assuming equimolar concentrations of the five constituent oxides in (CoCuMgNiZn)O are also listed in darker shades of blue and orange. The range of experimental values measured in this study for bulk consolidated single-phase equimolar TM-HEO are represented by the blue and orange shaded regions for hardness and elastic modulus respectively. Note the logarithmic scale on the y-axis.

4.3. Composite model analysis

The mechanical properties of ceramics are known to be highly sensitive to grain size [41]. One of the primary grain size effects is due to Hall-Petch strengthening, although changes in the relative contributions of different microstructural features (i.e., grains, grain boundaries, and triple points) and deformation mechanisms can also influence the mechanical properties. Assuming the material does not undergo any chemical or structural transformations, the thickness of the grain boundaries and the size of the triple points is thought to remain constant as grain size decreases. As such, as the grain size decreases, the relative volume fraction of grain boundaries and triple points will increase, relative to the grain interior. Grain boundaries and triple points are thought to be mechanically more fragile than the grain interior [43], resulting in the mechanical properties of a ceramic being highly dependent on the volume fraction of the various microstructure features. A few different models can be used in conjunction to estimate the influence of these microstructure features on the mechanical behavior of polycrystalline ceramics. The first model considered in this study is the Chaim composite model, which can be used to calculate the volume fractions of different microstructural features [43]. Secondly, the Hill composite estimation (HCE) method approximates mechanical properties on the basis of the respective volume fractions of the grain interiors and the intercrystalline regions (grain boundaries and triple points) [41, 43,44]. Lastly, the well-established Hall-Petch relationship is commonly believed to strengthen polycrystalline materials on the basis of dislocation pileup at grain boundaries.

The Chaim composite model allows for the microstructure of a ceramic to be modeled as a composite consisting of grain interiors, grain boundaries between two grains, and triple points between three grains [43]. It is possible to calculate the volume fraction of the grain bulk and intercrystalline regions, respectively, by modeling each grain as a tetrakaidecahedron. The model detailed by Chaim [43] estimates the volume fraction of the grain interior, V_g , as:

$$V_g = \left(1 - \frac{3}{\sqrt{6}} \bullet \frac{\lambda}{d}\right)^3 \tag{3}$$

where d is the grain size and λ is the grain boundary thickness. The volume fraction of the intercrystalline region, V_i , can then be calculated as:

$$V_i = 1 - V_g \tag{4}$$

Furthermore, x is a function used to simplify the relation between grain size and grain boundary thickness in a tetrakaidekahedron system by:

$$x = \frac{3}{\sqrt{6}} \bullet \frac{\lambda}{d} \tag{5}$$

Thus, the intracrystalline component, including the grain boundary volume fraction (V_{gb}), can be defined as:

$$V_{gb} = 3x(1-x)^2 (6)$$

and the triple point fraction (V_{tp}) defined as:

$$V_{p} = 3x^{2}(1-x) \tag{7}$$

Using Eqs. 3–7, it is possible to estimate the relative volume fractions of the grain and intercrystalline features that constitute the microstructure of bulk single-phase TM-HEO as the grain size changes. For this analysis, a value of $\lambda=2$ nm was used based on fitting of the hardness data using the HCE method (as discussed below). The λ value of 2 nm is also consistent with TEM imaging [45]. The estimated volume fraction of each microstructural component is illustrated in Fig. 6 (note the logarithmic scale on the x-axis). The estimated volume fraction of the intercrystalline region is negligible at larger grain sizes but increases significantly as the grain size is reduced. For instance, for a grain size of 0.10 μm , the volume fraction of the intercrystalline region is approximately 10 %, whereas the estimated value increases to approximately 50 % for a grain size of approximately 0.012 μm , at which point the volume fractions of the grain interior and intercrystalline region are roughly equal.

The mechanical properties for both coarse and nanocrystalline grain sizes can be assessed using the method introduced by Ehre and Chaim, which estimates the bulk mechanical properties using the tetrakaide-cahedron model and the HCE [41,43]. The HCE takes into account the models of Reuss and Voigt, which represent the lower (T_{Reuss}) and upper (T_{Voigt}) bounds, respectively, of property T [43]:

$$(T_{Reuss})^{-1} = \Sigma V_n / T_n$$
 (8)

$$T_{Voigt} = \Sigma V_n \bullet T_n \tag{9}$$

where T_n is the corresponding property of component n, and V_n is the volume fraction of component n. For polycrystalline materials, the

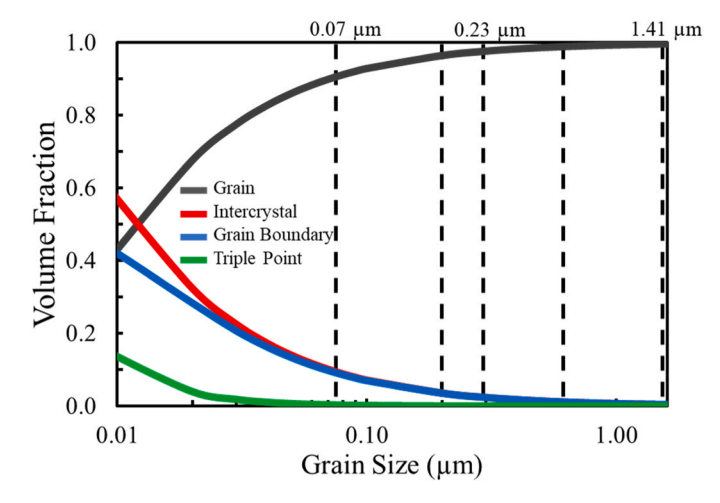


Fig. 6. Estimated volume fraction of grain interiors (grey) and intercrystalline regions (red) with respect to grain size using the Chaim model [43] and an assumed grain boundary thickness value of 2 nm. Grain boundary (blue) and triple point (green) volume fractions, which make up the intercrystalline regions, are also shown. Note the logarithmic scale on the x-axis. Average grain size values relevant to this study are represented by black dashed lines.

effective property usually lies in between these two bounds [43,44]. Averaging these upper and lower bounds, it is possible to estimate the hardness using the following HCE equation:

$$H_{Hill} = 0.5 \left(\left(\frac{V_g}{H_g} + \frac{V_i}{H_i} \right)^{-1} + V_g \bullet H_g + V_i \bullet H_i \right)$$
 (10)

where H_{Hill} is the HCE value for hardness, H_g is the hardness of the grain interior, and H_i is the hardness of the intercrystalline region [43].

Whereas values for V_g and V_i can be estimated using the Chaim composite model, described above, values for H_g and H_i are still needed. To calculate H_g , we can consider the properties when the grain size is sufficiently large, such that the volume fraction of the intercrystalline region can be considered negligible, and the hardness can be attributed only to the hardness of the grain interior. The H_g value can thus be approximated by applying the Hall-Petch equation, below, assuming coarse grain sizes:

$$H_{H-P} = H_0 + \frac{k}{\sqrt{d}} \tag{11}$$

where H_0 and k are material constants [46]. We can estimate these material constants by fitting samples SPS800, SPS850, and SPS900 to Eq. 11, which yields $H_0 = 5.9 \,\mathrm{GPa}$ and $k = 53.6 \,\mathrm{GPa} \,\mathrm{nm}^{1/2}$ (or 1.7 GPa μ m^{1/2}). Our H_0 and k values are within the same order of magnitude as those used for oxides such as MgO ($H_0 = 6.5$ GPa and k =3.0 GPa μ m^{1/2}), MgAl₂O₄ (10.9 GPa, 58.62 GPa nm^{1/2}), and Al₂SiO₅ (19.7 GPa, 40.0 GPa nm $^{1/2}$) [41,47,48]. For grain sizes larger than approximately 1 μ m, the value of H_{H-P} becomes relatively constant, and can be assumed equal to H_0 and H_g , at a value of ~ 6 GPa. Previous studies have further estimated $H_i \approx 0.5H_g$ [41], giving us a value for H_i of ~3 GPa, which is consistent with the expected decrease in hardness of the intercrystalline region compared to the grain interior. Applying these values in Eq. 10 allows for an estimation of the hardness, assuming the HCE model, as shown in Fig. 7, denoted in red. The hardness is predicted to be relatively constant for larger grain sizes due to the small volume fraction of intercrystalline regions, decreasing notably when the grain size is less than approximately 0.05 µm.

Also shown in Fig. 7 are the measured hardness values and two additional sets of estimated values: (1) using the Hall-Petch model (in gray), and (2) using the Hall-Petch and HCE models together (in orange). The Hall-Petch curve utilizes Eq. 11 and presents a monotonic

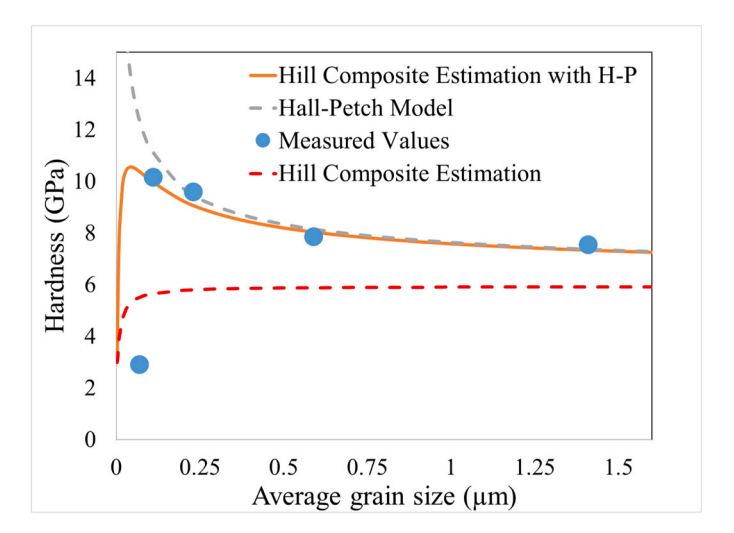


Fig. 7. Hardness vs average grain size for bulk consolidated single-phase TM-HEO samples, measured experimentally (blue circles) and calculated using the Hall-Petch relationship (dashed gray line), the Hill composite estimation (red line), and the Hill composite estimation in combination with Hall-Petch strengthening model (orange line).

increase in hardness with decreasing average grain size. By combining Eqs. 10 and 11, the hardness is estimated to increase with decreasing grain size at grain sizes >0.04 µm due to the contribution of the Hall-Petch strengthening (Eq. 11) and the small volume fraction of intercrystalline regions ($V_i < 0.17$ for AGS $> 0.04 \,\mu\text{m}$). The hardness continues to increase until a critical grain size is reached, which the model predicts to be \sim 0.04 μm for our single-phase TM-HEO. Below this critical grain size, the contribution of the mechanically weaker intercrystalline region begins to dominate, leading to the precipitous drop in the calculated hardness values. Notably, the combined model presents data trends similar to those observed in the measured values, except the critical grain size value for peak hardness is lower for the estimated values ($\sim 0.04 \, \mu m$) compared to those for the measured values (~0.07–0.11 μ m). Adjustments to predefined variable parameters, like λ or H_i, enable the model to converge towards 0.11 µm. However, this leads to significant deviations from the Hall-Petch portion of the HCE. Although the values in the model are approximations and are therefore not expected to exactly match the empirical data, this divergence at small grain sizes suggests that the presence of the weaker intercrystalline region does not fully explain the decrease in hardness at small grain sizes, thus additional mechanisms are considered below.

4.4. Grain size dependence of hardness and elastic modulus

To evaluate deformation mechanisms contributing to hardness and elastic modulus properties, it is helpful to separate samples into two regimes: those with average grain size values greater than the critical grain size, and those with values less than the critical grain size. The former are expected to exhibit Hall-Petch behavior, whereas the latter are defined to inverse Hall-Petch behavior. The transition in behavior for the samples in this study occurs at a critical grain size in the range of 0.075–0.11 μm (see Fig. 4 and Fig.8). Hall-Petch behavior has been observed before in other oxide materials such as MgO [41], MgAl₂O₄ [29], Al₂O₃ [49], and Al₂O₃ / SiO₂ composites [47]. Several of these materials exhibit an inverse Hall-Petch relationship with critical grain size values as follows: MgO \sim 0.130 μm , MgAl₂O₄ \sim 0.018 μm , and Al₂O₃ / SiO₂ composites \sim 0.081 μm , respectively [29,41,47]. The critical grain size exhibited for our bulk single-phase TM-HEO samples most

closely resembles the value observed for MgO, which is unsurprising given that MgO is a constituent in the composition used in this study and has the same crystal structure (rocksalt) and bonding type (ionic).

Sample SPS900, having the largest grain size in this study (1.4 μm), exhibits a hardness value of 7.5 GPa. As the average grain size decreases, the hardness increases until a grain size of 0.11 µm. The increase in strength can be attributed to the increasing concentration of grain boundaries with decreasing grain size, which act as barriers to dislocation motion [50,51]. For average grain sizes less than approximately $0.11~\mu m$, the hardness values begin to decrease. A decrease in hardness with decreasing grain size is indicative of an inverse Hall-Petch behavior [50,51], which is often attributed to grain boundary sliding and nanocracking associated with the increasing grain boundary concentration and increasing number of triple points at smaller grain sizes [29,41,52]. A study published by Ratzker et al. corroborates that grain boundary sliding and rotation may also contribute to inverse Hall-Petch behavior [30]. Similar deformation mechanisms are apparent in our previous scratch tests for single-phase TM-HEO samples with variable grain sizes [34]. Micron grain size single-phase TM-HEO deforms through dislocation slip, while nano grain size single-phase TM-HEO exhibits grain boundary sliding and nanocracking [34]. We propose that the emergence of an inverse Hall-Petch behavior in our bulk single-phase TM-HEO samples is related to the increased prevalence for nanocracking at small grain sizes from triple points. The observed Hall-Petch and inverse Hall-Petch behavior, demonstrated by increasing and decreasing hardness, highlights the significance of how grain size and grain boundary response influence the TM-HEO's mechanical properties.

Similar to our hardness data, the elastic modulus values for the bulk single-phase TM-HEO can be divided into two distinct grain size regimes. For grain sizes $\geq\!0.11$ µm, decreasing grain size results in an increase in elastic modulus. Elastic modulus is typically independent of grain size at large grain sizes [43,50]. Notably, Hong et al. have also observed a grain size dependent elastic behavior in bulk TM-HEO samples measured using three-point bending [31]. They attribute the increase in elastic modulus to the increase in grain size, as well as elemental segregation (note that their samples are not single-phase). Additionally, they observed a peak in elastic modulus at a grain size

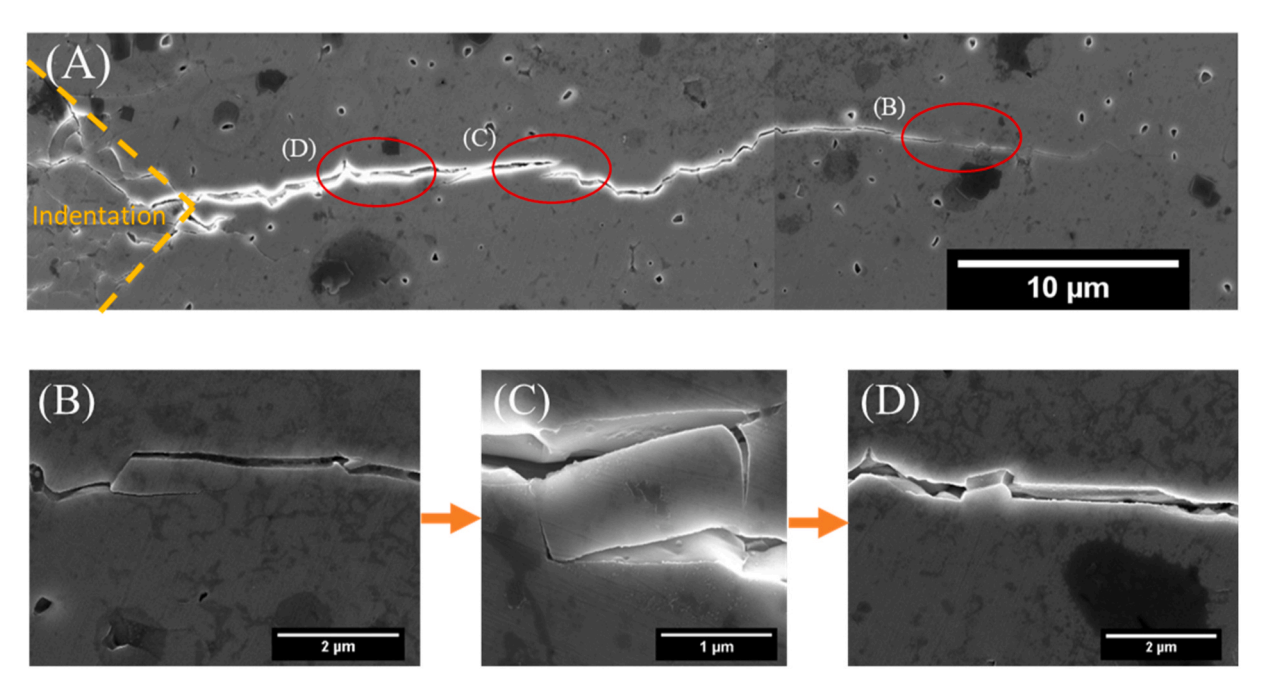


Fig. 8. (A) Scanning electron micrograph of a crack in bulk consolidated single-phase TM-HEO sample SPS900 (AGS = 1.4 µm) created during a fracture toughness measurement. Red circles highlight regions of observed grain bridging. (B-D) Magnified images of grain bridging phenomena, illustrating the stages of grain bridge development: (B) formation, (C) interlocking, (D) and rupture.

of 3.5 µm, followed by a decrease in elastic modulus with decreasing grain size due to the low relative density of the finer grained samples (≤ 94 % at AGS \leq 2.1 μm). Elastic modulus also can be influenced by porosity [53-55]. We note that our sample with the smallest grain size, which exhibits the lowest elastic modulus, also exhibits the lowest density (95.6 %). In an effort to deconvolute possible effects due to grain size from those due to porosity, we look closer at the literature on TM-HEO and MgO. In the study by Hong et al., their sample with a similar density value (95.6 %), which had an average grain size of $3.5 \mu m$, actually exhibited the peak elastic modulus value among their samples [31]. Other studies on MgO report a decrease in hardness and elastic modulus at a similar critical grain size value (0.130 µm), while having comparable relative density values to our measurements (94 -97 %) [41,56]. These additional studies support our determination that with a density of >95 %, grain size is the dominant variable controlling the observed changes in elastic modulus. While a similar grain size dependent elastic modulus trend in TM-HEO has now been observed using two different mechanical measurements techniques, more work is needed to fully understand the role of grain size and porosity on the elastic response in the nanocrystalline regime.

In contrast to the samples with grain sizes larger than the critical grain size, the elastic modulus decreases significantly in sample SPS700 (AGS = $0.075 \mu m$), indicating a change in elastic behavior at such small grain sizes. A similar decrease in elastic modulus below a critical grain size has been observed before in MgO (\sim 0.10 μ m) and ZrO₂-3 wt% Y₂O₃ $(\sim 0.06 \, \mu m)$ [56,57]. The decrease in elastic modulus at small grain sizes can be attributed to the increasing grain boundary concentration with decreasing grain size. The grain boundary will have a reduced elastic modulus compared to the grain interior [47,57,58]. For instance, Yeheskel et al. actually evaluated up to a threefold decrease in elastic modulus for grain boundaries in MgO [56]. Treating the samples as a composite of grain interiors and grain boundaries, such as through the application of the HCE model, will yield a meaningful decrease in elastic modulus when grain boundaries occupy a significant amount of the bulk volume. HCE-based estimates for elastic modulus for our TM-HEO samples highlight this behavior, as illustrated in Figure S2 in the supplemental materials.

4.5. Grain size dependance of fracture toughness

Fracture toughness in ceramics is complex, difficult to predict, and can be a strong function of processing, and microstructure. Additionally, results in the literature can be contradictory. For example, a previous study observed that the fracture toughness of alumina prepared through SPS was independent of average grain size [59]. Conversely, another study found that for hot pressed alumina, fracture toughness decreases with increasing average grain size [60]. Mechanisms that can influence the fracture toughness include but are not limited to: plastic deformation due to dislocation activity, intergranular or transgranular cracking, grain bridging, porosity, as well as the relative concentration of microstructural features such as grain boundaries and triple points [41, 61-63]. Our fracture toughness measurements indicate that fracture toughness generally increases with increasing average grain size in our single-phase TM-HEO samples (Fig. 4B). Ceramics exhibit a range of different relationships between toughness and grain size [64]. MgO, a constituent oxide in TM-HEO, has been shown to demonstrate a similar increase in fracture toughness with increasing average grain size, which the authors attribute to grain boundaries as a source of stress concentration and disparities in relative density [65].

In the present work, the final grain size of the bulk consolidated samples was controlled using SPS temperature, with higher temperatures yielding specimens with larger grain sizes. Higher sintering temperatures can also result in increased densification and reduced porosity in the densified samples. Porosity is known to influence fracture behavior, with greater amounts of porosity resulting in reduced fracture toughness [26]. However, the relative density values for all of our

samples are high (>95 %), and thus the observed increase in fracture toughness with increasing average grain size cannot be solely attributed to the effect of porosity. Based on data acquired here we propose fracture toughness in TM-HEO is dependent on average grain size, and attribute this to two factors, relative volume fraction of intercrystalline regions and the potential for grain bridging at larger grain sizes, as discussed below.

Fracture toughness is related to the ease with which a crack can propagate through a material under stress, with crack propagation being heavily influenced by the relative prevalence of transgranular and intergranular fracture. Intergranular fracture along grain boundaries requires less energy than transgranular fracture through grain interiors due to the lower fracture toughness of grain boundaries [66]. Fracture toughness often decreases with decreasing grain size due to limited dislocation activity, the increased prevalence of intergranular fracture, and the increasing concentration of grain boundaries in the microstructure [67]. Triple points can also play a role in the bulk fracture behavior of a material [68]. Stress concentrations at the triple point can lead to crack nucleation during mechanical loading. An increase in the number and volume fraction of triple points would, therefore, be expected to increase the propensity for crack formation and reduce the fracture toughness. Based on the Chaim composite model (Fig. 6), the volume fraction of intercrystalline region, including grain boundaries and triple points, is estimated to be 5.2×10^{-3} for a grain size of 1.4 μm and increases to 9.7×10^{-2} for a grain size of 0.075 µm. At our smallest grain size, 0.075 µm, we estimate an intercrystalline region concentration of almost 10 vol%, a significant portion of the microstructure. We, therefore, partially attribute our decline in fracture toughness with decreasing average grain size to the increased prevalence of intercrystalline fracture, defects, and nanocracking.

In addition to the indentation measurements and calculations described above, SEM micrographs were acquired on the indent-induced cracks to further explore the fracture toughness behavior. A representative crack for sample SPS900 (AGS $= 1.4 \mu m$) is shown in Fig. 8A. The crack is observed to propagate from the left side of Fig. 8A (at the edge of the Vickers indent) to the right side of the figure (the crack tip). The sample is observed to fracture primarily transgranularly. Additionally, significant grain bridging is observed in the crack (circled in red in Fig. 8A). Grain bridging is a common toughening mechanism that may also contribute to our observed fracture toughness behavior. It is believed this mechanism occurs when frictional interlocking forces slow crack growth as the grain begins to debond [69]. These frictional forces apply a closing force on the two crack surfaces, which requires additional energy to overcome to continue crack growth. The continuous activation of grain bridging events at the microscopic level will result in meaningful crack growth resistance and an observed increase in the measured fracture toughness. Alumina exhibits increasing fracture toughness with an increase in grain size, due to the increased likelihood of grain bridging [61,69,70]. Spinel MgAl₂O₄ is also known to exhibit grain bridging at larger grain sizes [62,63]. Larger grains offer increased closure forces between the two crack surfaces by means of frictional forces from grain bridging.

Grain bridging has been observed to be a multistep process, having a distinct beginning, middle and end [71]. Although we did not attempt to track the formation of grain bridging in real time, the propagation of a crack can be used as a proxy for the evolution in a grain bridge. The evolution in grain bridging behavior in this sample can be seen in Fig. 8B-D, and matches closely with what is observed in Al_2O_3 [69]. Fig. 8B highlights the beginning of a grain bridge formation, where crack reinitiation occurs on the other side of the grain. Fig. 8C shows the intermediate stage, where the grain still frictionally pulls the crack surfaces together. Here the crack surfaces have widened slightly more to reveal the entire grain shape just before the bridge ruptures. Lastly, in Fig. 8D, the crack has ruptured and separated in the later stages of propagation and a former bridged grain can be seen with the residual concave feature adjacent to it. The observation of the complete grain

bridging lifecycle indicates that the fracture behavior in the bulk single-phase TM-HEO samples is influenced by the presence, or absence, of grain-localized bridging elements. Although some limited grain bridging is observed in sample SPS700 (Figure S3), grain bridging and transgranular fracture are known to become less prevalent at smaller grain sizes [70]. We observe that cracks in sample SPS700 propagate primarily through intergranular fracture.

At this time, we cannot unambiguously decouple the role of the various microstructure features on the fracture behavior. However, from the above analysis, we assert that as grain size decreases, the grain boundary and triple point volume fractions will increase. This increase will introduce more defects and nanocrack nucleation sites that will play an increasingly detrimental role in the fracture behavior of our samples as the average grain size decreases. In addition to this, the absence of transgranular cracking and grain bridging at finer grain sizes appears to contribute to the significant decrease in toughness.

5. Conclusions

Bulk single-phase TM-HEO samples with a range of final grain sizes were successfully consolidated. Hardness and elastic modulus measurements of these samples showed a Hall-Petch relationship with grain size until a grain size of $\sim 0.11~\mu m$. The hardness decreases at grain sizes smaller than 0.11 µm due to nanocracking present at grain boundaries and triple points. Elastic modulus exhibits similar behavior, which is attributed to reduced elastic modulus of grain boundaries. Fracture toughness values assessed from indentation cracks exhibit a decrease in fracture toughness with decreasing grain size. Further investigation of the crack pathways revealed transgranular cracking with grain bridging as a possible toughening mechanism in the coarse grain samples and a prevalence of nanocracking at smaller grain sizes leading to a reduction in fracture toughness. The behavior is similar to that observed in previous studies of MgO, one of the constituent oxides in TM-HEO, which also forms the rocksalt crystal structure. Overall, the influence of grain size on key mechanical properties presented here suggests that microstructure can be used to tailor the mechanical behavior of bulk singlephase TM-HEOs for diverse applications. Conversely, grain size needs to be carefully controlled to ensure reproducible mechanical response.

CRediT authorship contribution statement

William J. Bowman: Formal analysis, Writing – review & editing. Timothy J. Rupert: Investigation, Writing – review & editing. Julie Schoenung: Conceptualization, Funding acquisition, Investigation, Resources, Supervision, Writing – review & editing. Justin Cortez: Conceptualization, Formal analysis, Validation, Writing – original draft, Writing – review & editing, Investigation. Alexander D. Dupuy: Conceptualization, Formal analysis, Funding acquisition, Investigation, Writing – review & editing. Hasti Vahidi: Investigation, Writing – review & editing. Olivia K. Donaldson: Investigation, Writing – review & editing.

Declaration of Competing Interest

The authors declare that they have no known competing financial interests or personal relationships that could have appeared to influence the work reported in this paper.

Acknowledgements

This research was primarily supported by the National Science Foundation (NSF) Materials Research Science and Engineering Center (MRSEC) through the UC Irvine Center for Complex and Active Materials (DMR-2011967) and additional support received from NSF award CMMI-2029966 (for ADD and JMS) and the Graduate Assistance in Areas of National Need (P200A-180043) (for JC). We also acknowledge

the use and access to equipment and facilities at the UC Irvine Materials Research Institute (IMRI) – (including funding from NSF DMR-2011967).

Appendix A. Supporting information

Supplementary data associated with this article can be found in the online version at doi:10.1016/j.jeurceramsoc.2024.116673.

References

- B. Cantor, I.T.H. Chang, P. Knight, A.J.B. Vincent, Microstructural development in equiatomic multicomponent alloys, Mater. Sci. Eng. A. 375–377 (2004) 213–218, https://doi.org/10.1016/j.msea.2003.10.257.
- [2] A.L. Greer, Confusion by design, Nature 366 (1993) 303–304, https://doi.org/ 10.1038/366303a0.
- [3] Y. Zhang, T.T. Zuo, Z. Tang, M.C. Gao, K.A. Dahmen, P.K. Liaw, Z.P. Lu, Microstructures and properties of high-entropy alloys, Prog. Mater. Sci. 61 (2014) 1–93, https://doi.org/10.1016/j.pmatsci.2013.10.001.
- [4] B.E. MacDonald, Z. Fu, B. Zheng, W. Chen, Y. Lin, F. Chen, L. Zhang, J. Ivanisenko, Y. Zhou, H. Hahn, E.J. Lavernia, Recent progress in high entropy alloy research, JOM 69 (2017) 2024–2031, https://doi.org/10.1007/s11837-017-2484-6.
- [5] E.J. Pickering, N.G. Jones, High-entropy alloys: a critical assessment of their founding principles and future prospects, Int. Mater. Rev. 61 (2016) 183–202, https://doi.org/10.1080/09506608.2016.1180020.
- [6] J.-W. Yeh, S.-K. Chen, S.-J. Lin, J.-Y. Gan, T.-S. Chin, T.-T. Shun, C.-H. Tsau, S.-Y. Chang, Nanostructured high-entropy alloys with multiple principal elements: novel alloy design concepts and outcomes, Adv. Eng. Mater. 6 (2004) 299–303, https://doi.org/10.1002/ADEM.200300567.
- [7] C.M. Rost, E. Sachet, T. Borman, A. Moballegh, E.C. Dickey, D. Hou, J.L. Jones, S. Curtarolo, J. Maria, Entropy-stabilized oxides, Nat. Commun. 6 (1) (2015) 8, https://doi.org/10.1038/ncomms9485.
- [8] A. Mao, H.Z. Xiang, Z.G. Zhang, K. Kuramoto, H. Yu, S. Ran, Solution combustion synthesis and magnetic property of rock-salt (Co_{0.2} Cu_{0.2} Mg_{0.2} Ni_{0.2} Zn_{0.2})O high-entropy oxide nanocrystalline powder, J. Magn. Magn. Mater. 484 (2019) 245–252, https://doi.org/10.1016/j.jmmm.2019.04.023.
- [9] A. Sarkar, R. Djenadic, N.J. Usharani, K.P. Sanghvi, V.S.K. Chakravadhanula, A. S. Gandhi, H. Hahn, S.S. Bhattacharya, Nanocrystalline multicomponent entropy stabilised transition metal oxides, J. Eur. Ceram. Soc. 37 (2017) 747–754, https://doi.org/10.1016/j.jeurceramsoc.2016.09.018.
- [10] M.R. Chellali, A. Sarkar, S.H. Nandam, S.S. Bhattacharya, B. Breitung, H. Hahn, L. Velasco, On the homogeneity of high entropy oxides: an investigation at the atomic scale, Scr. Mater. 166 (2019) 58–63, https://doi.org/10.1016/j. scriptamat.2019.02.039.
- [11] A.D. Dupuy, M.R. Chellali, H. Hahn, J.M. Schoenung, Multiscale phase homogeneity in bulk nanocrystalline high entropy oxides, J. Eur. Ceram. Soc. 41 (2021) 4850–4858, https://doi.org/10.1016/j.jeurceramsoc.2021.03.035.
- [12] R. Djenadic, A. Sarkar, O. Clemens, C. Loho, M. Botros, V.S.K. Chakravadhanula, C. Kübel, S.S. Bhattacharya, A.S. Gandhi, H. Hahn, Multicomponent equiatomic rare earth oxides, Mater. Res. Lett. 5 (2017) 102–109, https://doi.org/10.1080/ 21663831.2016.1220433.
- [13] S. Jiang, T. Hu, J. Gild, N. Zhou, J. Nie, M. Qin, T. Harrington, K. Vecchio, J. Luo, A new class of high-entropy perovskite oxides, Scr. Mater. 142 (2018) 116–120, https://doi.org/10.1016/j.scriptamat.2017.08.040.
- [14] J. Gild, Y. Zhang, T. Harrington, S. Jiang, T. Hu, M.C. Quinn, W.M. Mellor, N. Zhou, K. Vecchio, J. Luo, High-Entropy Metal Diborides: A New Class of High-Entropy Materials and a New Type of Ultrahigh Temperature Ceramics, Sci. Rep. 6 (2016) 2–11, https://doi.org/10.1038/srep37946.
- [15] X. Yan, L. Constantin, Y. Lu, J.F. Silvain, M. Nastasi, B. Cui, Hf_{0.2}Zr_{0.2}Ta_{0.2}Nb_{0.2}Ti_{0.2})C high-entropy ceramics with low thermal conductivity, J. Am. Ceram. Soc. 101 (2018) 4486–4491. https://doi.org/10.1111/jace.15779.
- [16] A.L. Vyatskikh, B.E. MacDonald, A.D. Dupuy, E.J. Lavernia, J.M. Schoenung, H. Hahn, High entropy silicides: CALPHAD-guided prediction and thin film fabrication, Scr. Mater. 201 (2021) 113914, https://doi.org/10.1016/J. SCRIPTAMAT.2021.113914.
- [17] J.L. Braun, C.M. Rost, M. Lim, A. Giri, D.H. Olson, G.N. Kotsonis, G. Stan, D. W. Brenner, J.P. Maria, P.E. Hopkins, Charge-induced disorder controls the thermal conductivity of entropy-stabilized oxides, Adv. Mater. 30 (2018), https://doi.org/10.1002/adma.201805004.
- [18] A. Sarkar, L. Velasco, D. Wang, Q. Wang, G. Talasila, L. de Biasi, C. Kübel, T. Brezesinski, S.S. Bhattacharya, H. Hahn, B. Breitung, High entropy oxides for reversible energy storage, Nat. Commun. 9 (2018), https://doi.org/10.1038/ s41467-018-05774-5.
- [19] A.D. Dupuy, I.-T. Chiu, P. Shafer, E. Arenholz, Y. Takamura, J.M. Schoenung, Hidden transformations in entropy-stabilized oxides, J. Eur. Ceram. Soc. (2021), https://doi.org/10.1016/j.jeurceramsoc.2021.06.014.
- [20] D. Bérardan, S. Franger, A.K. Meena, N. Dragoe, Room temperature lithium superionic conductivity in high entropy oxides, J. Mater. Chem. A. 4 (2016) 9536–9541, https://doi.org/10.1039/c6ta03249d.
- [21] N. Qiu, H. Chen, Z. Yang, S. Sun, Y. Wang, Y. Cui, A high entropy oxide $(Mg_{0.2}Co_{0.2}Ni_{0.2}Cu_{0.2}Zn_{0.2}O) \mbox{ with superior lithium storage performance, J. Alloy. Compd. 777 (2019) 767–774, https://doi.org/10.1016/j.jallcom.2018.11.049.}$

- [22] K. Wang, W. Hua, X. Huang, D. Stenzel, J. Wang, Z. Ding, Y. Cui, Q. Wang, H. Ehrenberg, B. Breitung, C. Kübel, X. Mu, Synergy of cations in high entropy oxide lithium ion battery anode, Nat. Commun. 14 (1) (2023) 9, https://doi.org/ 10.1038/s41467-073-37034-6
- [23] J.G. Thakare, C. Pandey, M.M. Mahapatra, R.S. Mulik, Thermal barrier coatings—a state of the art review, Met. Mater. Int. 27 (2021) 1947–1968, https://doi.org/ 10.1007/s12540-020-00705-w
- [24] J.C. Stallard, L. Wheatcroft, S.G. Booth, R. Boston, S.A. Corr, M.F. De Volder, B. J. Inkson, N.A. Fleck, Mechanical properties of cathode materials for lithium-ion batteries, Joule 6 (2022) 984–1007, https://doi.org/10.1016/j.joule.2022.04.001.
- [25] R.W. Rice, Comparison of stress concentration versus minimum solid area based mechanical property-porosity relations, J. Mater. Sci. 28 (1993) 2187–2190, https://doi.org/10.1007/BF00367582.
- [26] F.P. Knudsen, Dependence of mechanical strength of brittle polycrystalline specimens on porosity and grain size, J. Am. Ceram. Soc. 42 (1959) 376–387, https://doi.org/10.1111/J.1151-2916.1959.TB13596.X.
- [27] E.O. Hall, The deformation and ageing of mild steel: III Discussion of results, Proc. Phys. Soc. Sect. B. 64 (1951) 747–753, https://doi.org/10.1088/0370-1301/64/9/303
- [28] N.J. Petch, The cleavage strength of polycrystals, J. Iron Steel Inst. 174 (1953) 25–28
- [29] H. Ryou, J.W. Drazin, K.J. Wahl, S.B. Qadri, E.P. Gorzkowski, B.N. Feigelson, J. A. Wollmershauser, Below the hall-petch limit in nanocrystalline ceramics, ACS Nano 12 (2018) 3083–3094, https://doi.org/10.1021/acsnano.7b07380.
- [30] B. Ratzker, A. Wagner, M. Sokol, L. Meshi, S. Kalabukhov, N. Frage, Deformation in nanocrystalline ceramics: a microstructural study of MgAl₂O₄, Acta Mater. 183 (2020) 137–144, https://doi.org/10.1016/j.actamat.2019.11.015.
- [31] W. Hong, F. Chen, Q. Shen, Y.H. Han, W.G. Fahrenholtz, L. Zhang, Microstructural evolution and mechanical properties of (Mg,Co,Ni,Cu,Zn)O high-entropy ceramics, J. Am. Ceram. Soc. 102 (2019) 2228–2237, https://doi.org/10.1111/jace.16075.
- [32] K.C. Pitike, A.E. Marquez-Rossy, A. Flores-Betancourt, D.X. Chen, K.C. Santosh, V. R. Cooper, E. Lara-Curzio, On the elastic anisotropy of the entropy-stabilized oxide (Mg, Co, Ni, Cu, Zn)O compound, J. Appl. Phys. 128 (2020), https://doi.org/10.1063/5.0011352.
- [33] J. Chen, W. Liu, J. Liu, X. Zhang, M. Yuan, Y. Zhao, J. Yan, M. Hou, J. Yan, M. Kunz, N. Tamura, H. Zhang, Z. Yin, Stability and compressibility of cation-doped high-entropy oxide MgCoNiCuZnO₅, J. Phys. Chem. C. 123 (2019) 17735–17744, https://doi.org/10.1021/acs.jpcc.9b04992.
- [34] X. Wang, J. Cortez, A.D. Dupuy, J.M. Schoenung, W.J. Bowman, High entropy oxide (Co,Cu,Mg,Ni,Zn)O exhibits grain size dependent room temperature deformation, Mater. Res. Lett. 11 (2023) 196–204, https://doi.org/10.1080/ 21663831,2022,2135409.
- [35] C.M. Rost, D.L. Schmuckler, C. Bumgardner, M.S. Bin Hoque, D.R. Diercks, J. T. Gaskins, J.P. Maria, G.L. Brennecka, X. Li, P.E. Hopkins, On the thermal and mechanical properties of Mg_{0.2}Co_{0.2}Ni_{0.2}Cu_{0.2}Zn_{0.2}O across the high-entropy to entropy-stabilized transition, APL Mater. 10 (2022), https://doi.org/10.1063/5.01207775
- [36] C.A. Schneider, W.S. Rasband, K.W. Eliceiri, NIH Image to ImageJ: 25 years of image analysis, Nat. Methods 9 (2012) 671–675, https://doi.org/10.1038/ nmeth.2089.
- [37] A.L. Horovistiz, J.R. Frade, L.R.O. Hein, Comparison of fracture surface and plane section analysis for ceramic grain size characterisation, J. Eur. Ceram. Soc. 24 (2004) 619–626, https://doi.org/10.1016/S0955-2219(03)00260-7.
- [38] K. Niihara, R. Morena, D.P.H. Hasselman, Evaluation of K_{Ic} of brittle solids by the indentation method with low crack-to-indent ratios, J. Mater. Sci. Lett. 1 (1982) 13–16. https://doi.org/10.1007/BF00724706.
- [39] Z. Li, A. Ghosh, A.S. Kobayashi, R.C. Bradt, Indentation Fracture Toughness of Sintered Silicon Carbide in the Palmqvist Crack Regime, J. Am. Ceram. Soc. 72 (1989) 904–911, https://doi.org/10.1111/j.1151-2916.1989.tb06242.x.
- [40] A.D. Dupuy, X. Wang, J.M. Schoenung, Entropic phase transformation in nanocrystalline high entropy oxides, Mater. Res. Lett. 7 (2019) 60–67, https://doi. org/10.1080/21663831.2018.1554605.
- [41] D. Ehre, R. Chaim, Abnormal Hall-Petch behavior in nanocrystalline MgO ceramic, J. Mater. Sci. 43 (2008) 6139–6143, https://doi.org/10.1007/s10853-008-2936-z.
- [42] G.V. Samsonov, The Oxide Handbook, Springer US, 1973.
- [43] R. Chaim, Percolative composite model for prediction of the properties of nanocrystalline materials, J. Mater. Res. 12 (1997) 1828–1836, https://doi.org/ 10.1557/JMR.1997.0251.
- [44] R. Hill, The elastic behaviour of a crystalline aggregate, Proc. Phys. Soc. Sect. A. 65 (1952) 349–354, https://doi.org/10.1088/0370-1298/65/5/307.
- [45] H. Vahidi, A.D. Dupuy, B.X. Lam, J. Cortez, P. Garg, T.J. Rupert, J.M. Schoenung, W.J. Bowman, Reversible enhancement of electronic conduction caused by phase transformation and interfacial segregation in an entropy-stabilized oxide, Adv. Funct. Mater. (2024) 2315895, https://doi.org/10.1002/adfm.202315895.
- [46] I.J. McColm, Ceramic hardness, Springer New York, NY. (1990). https://doi.org/ https://doi.org/10.1007/978-1-4757-4732-4.
- [47] N.A. Gaida, N. Nishiyama, A. Masuno, A. Holzheid, H. Ohfuji, U. Schürmann, C. Szillus, E. Kulik, J. Bednarcik, O. Beermann, C. Giehl, L. Kienle, Synthesis of Al₂O₃/SiO₂ nano-nano composite ceramics under high pressure and its inverse

- Hall-Petch behavior, J. Am. Ceram. Soc. 100 (2017) 323–332, https://doi.org/10.1111/jace.14551.
- [48] E. Novitskaya, K. Karandikar, K. Cummings, M. Mecartney, O.A. Graeve, Hall-Petch effect in binary and ternary alumina / zirconia / spinel composites, J. Mater. Res. Technol. 11 (2021) 823–832, https://doi.org/10.1016/j.jmrt.2021.01.058.
- [49] L. Huang, W. Yao, A.K. Mukherjee, J.M. Schoenung, Improved mechanical behavior and plastic deformation capability of ultrafine grain alumina ceramics, J. Am. Ceram. Soc. 95 (2012) 379–385, https://doi.org/10.1111/J.1551-2916.2011.04951.X.
- [50] K. Kadau, T.C. Germann, P.S. Lomdahl, B.L. Holian, D. Kadau, P. Entel, M. Kreth, F. Westerhoff, D.E. Wolf, Mol. -Dyn. Study Mech. Deform. Nano-Cryst. Alum. (2004), https://doi.org/10.1007/s11661-004-0217-2.
- [51] P.-K. Huang, J.-W. Yeh, Effects of substrate bias on structure and mechanical properties of (AlCrNbSiTiV)N coatings, J. Phys. D. Appl. Phys. 42 (2009) 115401, https://doi.org/10.1088/0022-3727/42/11/115401.
- [52] C.E. Carlton, P.J. Ferreira, What is behind the inverse Hall-Petch effect in nanocrystalline materials? Acta Mater. 55 (2007) 3749–3756, https://doi.org/ 10.1016/j.actamat.2007.02.021.
- [53] E.A. Dean, J.A. Lopez, Empirical Dependence of Elastic Moduli on Porosity for Ceramic Materials, J. Am. Ceram. Soc. 66 (1983) 366–370, https://doi.org/ 10.1111/j.1151-2916.1983.tb10051.x.
- [54] M. Asmani, C. Kermel, A. Leriche, M. Ourak, Influence of porosity on Youngs modulus and poisson's ratio in alumina ceramics, J. Eur. Ceram. Soc. 21 (2001) 1081–1086, https://doi.org/10.1016/S0955-2219(00)00314-9.
- [55] J. Luo, R. Stevens, Porosity-dependence of elastic moduli and hardness of 3Y-TZP ceramics, Ceram. Int. 25 (1999) 281–286, https://doi.org/10.1016/S0272-8842 (98)00037-6.
- [56] O. Yeheskel, R. Chaim, Z. Shen, M. Nygren, Elastic moduli of grain boundaries in nanocrystalline MgO ceramics, J. Mater. Res. 20 (2005) 719–725, https://doi.org/ 10.1557/JMR.2005.0094.
- [57] R. Chaim, M. Hefetz, Effect of grain size on elastic modulus and hardness of nanocrystalline ZrO₂-3 wt% Y₂O₃ ceramic, J. Mater. Sci. 39 (2004) 3057–3061, https://doi.org/10.1023/B;JMSC,0000025832.93840.b0.
- [58] D. Chen, Computer model simulation study of nanocrystalline iron, Mater. Sci. Eng. A. 190 (1995) 193–198, https://doi.org/10.1016/0921-5093(94)09597-P.
- [59] W. Yao, J. Liu, T.B. Holland, L. Huang, Y. Xiong, J.M. Schoenung, A.K. Mukherjee, Grain size dependence of fracture toughness for fine grained alumina, Scr. Mater. 65 (2011) 143–146, https://doi.org/10.1016/J.SCRIPTAMAT.2011.03.032.
- [60] T. Tani, Y. Miyamoto, M. Koizumi, M. Shimada, Grain size dependences of vickers microhardness and fracture toughness in Al₂O₃ and Y₂O₃ ceramics, Ceram. Int. 12 (1986) 33–37, https://doi.org/10.1016/S0272-8842(86)80007-4.
- [61] S.J. Bennison, B.R. Lawn, Role of interfacial grain-bridging sliding friction in the crack-resistance and strength properties of nontransforming ceramics, Acta Met. 37 (1989) 2659–2671. https://doi.org/10.1016/0001-6160(89)90299-X.
- [62] J.C. Hay, K.W. White, Crack face bridging mechanisms in monolithic MgAl₂O₄ spinel microstructures, Acta Metall. Mater. 40 (1992) 3017–3025, https://doi.org/10.1016/0956-7151(92)90465-O.
- [63] M. Sakai, R.C. Bradt, A.S. Kobayashi, Toughness of polycrystalline MgAl₂O₄, Nippon Seramikkusu Kyokai Gakujutsu Ronbunshi/, J. Ceram. Soc. Jpn. 96 (1988) 525–531, https://doi.org/10.2109/jcersj.96.525.
- [64] R.W. Rice, S.W. Freiman, P.F. Becher, Grain-Size Dependence of Fracture Energy in Ceramics: I, Experiment, J. Am. Ceram. Soc. 64 (1981) 345–350, https://doi.org/ 10.1111/j.1151-2916.1981.tb10300.x.
- [65] Y. Wei, S. Gu, H. Fang, W. Luo, X. Zhang, L. Wang, W. Jiang, Properties of MgO transparent ceramics prepared at low temperature using high sintering activity MgO powders, J. Am. Ceram. Soc. 103 (2020) 5382–5391, https://doi.org/10.1111/JACE.17267.
- [66] S.M. Taheri Mousavi, N. Richart, C. Wolff, J.F. Molinari, Dynamic crack propagation in a heterogeneous ceramic microstructure, insights from a cohesive model, Acta Mater. 88 (2015) 136–146, https://doi.org/10.1016/J. ACTAMAT.2015.01.003.
- [67] B. Mussler, M.V. Swain, N. Claussen, Dependence of Fracture Toughness of Alumina on Grain Size and Test Technique, J. Am. Ceram. Soc. 65 (1982) 566–572, https://doi.org/10.1111/j.1151-2916.1982.tb10783.x.
- [68] S. Kobayashi, T. Inomata, H. Kobayashi, S. Tsurekawa, T. Watanabe, Effects of grain boundary- and triple junction-character on intergranular fatigue crack nucleation in polycrystalline aluminum, J. Mater. Sci. 43 (2008) 3792–3799, https://doi.org/10.1007/s10853-007-2236-z.
- [69] P.L. Swanson, C.J. Fairbanks, B.R. Lawn, Y. -W. Mai, B.J. Hockey, Crack-Interface Grain Bridging as a Fracture Resistance I, Mechanism in Ceramics: I, Experimental Study on Alumina, J. Am. Ceram. Soc. 70 (1987) 279–289, https://doi.org/ 10.1111/j.1151-2916.1987.tb04982.x.
- [70] T. Koyama, A. Nishiyama, K. Niihara, Effect of grain morphology and grain size on the mechanical properties of Al_2O_3 ceramics, J. Mater. Sci. 29 (1994) 3949–3954, https://doi.org/10.1007/BF00355953.
- [71] J.W. Foulk Iii, R.M. Cannon, G.C. Johnson, P.A. Klein, R.O. Ritchie, A micromechanical basis for partitioning the evolution of grain bridging in brittle materials, J. Mech. Phys. Solids (2007), https://doi.org/10.1016/j. jmps.2006.10.009.